Full-Scale Shake Table Test Damage Data Collection Using Terrestrial Laser Scanning Techniques

Mohammad Aghababaei[1], Christian Okamoto[2], Maria Koliou[3*], Takuya Nagae[4], Chris P. Pantelides[5], Keri L. Ryan[6], Andre R. Barbosa[7], Shiling Pei[8], John W. van de Lindt[9], Shideh Dashti[10]

Abstract

This paper presents the use of modern survey techniques, particularly Light Detection and Ranging (LiDAR) scanning to collect time-sensitive information before and after shake table experiments. Two full-scale three-story residential buildings were tested simultaneously on the largest shake table in the world. The focus of this study is on the use of LiDAR to document observations during these tests. The challenges experienced during this study prompted the development of a formalized survey procedure using LiDAR scanning techniques, which can be used by other researchers when planning to collect such time-sensitive data from similar experimental programs. In this paper, damage assessment through visual inspection, which is commonly performed during

[1] Ph.D. Student and Graduate Research Assistant, Zachry Department of Civil and Environmental Engineering, Texas A&M University, College Station, TX, 77843, U.S.A., E-mail: mohammad.aghababaei@tamu.edu

[2] Former Undergraduate Student, Zachry Department of Civil and Environmental Engineering, Texas A&M University, College Station, TX, 77843, U.S.A., E-mail: christianokamoto18@tamu.edu

[3] Assistant Professor, Zachry Department of Civil and Environmental Engineering, Texas A&M University, College Station, TX, 77843, U.S.A., E-mail: maria.koliou@tamu.edu (*Corresponding author)

[4] Associate Professor, Disaster Mitigation Research Center, Nagoya University, Nagoya, Japan, E-mail: nagae@ngoya-u.jp

[5] Professor, Department of Civil and Environmental Engineering, University of Utah, Salt Lake City, UT, 84112, U.S.A., E-mail: c.pantelides@utah.edu

[6] Associate Professor, Department of Civil and Environmental Engineering, University of Nevada Reno, Reno, NV, 89557, U.S.A., Email: klryan@unr.edu

[7] Associate Professor, School of Civil and Construction Engineering, Oregon State University, Corvallis, OR, 97331, U.S.A., Email: andre.barbosa@oregonstate.edu

[8] Associate Professor, Department of Civil and Environmental Engineering, Colorado School of Mines, Golden, CO, 80401, U.S.A., Email: spei@mines.edu

[9] Harold H. Short Endowed Chair Professor and Co-Director – Center of Excellence for Risk-Based Community Resilience Planning, Department of Civil and Environmental Engineering, Colorado State University, Fort Collins, CO, 80523, U.S.A., E-mail: jwv@colostate.edu

[10] Associate Professor, Department of Civil, Environmental and Architectural Engineering, University of Colorado Boulder, Boulder, CO, 80309, U.S.A., Email: shideh.dashti@colorado.edu

full-scale tests, is compared to post-experiment assessments using post-processed LiDAR derived point clouds. Various examples of damage to structural and nonstructural components, including columns, bracing, partition walls, and façades, are illustrated through post-shaking visual inspections as well as LiDAR derived point clouds. The feasibility of making accurate measurements using LiDAR point clouds, and automatically detecting damage using the point-to-point cloud comparison is presented. Finally, the relationship between observations through traditional instruments (e.g., accelerometers, laser meters, etc.) and LiDAR is discussed. In one example, the measurements from eight laser meters around the buildings are used to validate the measurements obtained using LiDAR point clouds. It is concluded that observations through LiDAR are complementary to those from traditional instruments, while permanent/residual displacements after the tests can be measured from both traditional and modern instruments.

Keywords: *Damage, Full-scale Shake Table Tests, Terrestrial Laser Scanning*, *LiDAR, Wood Buildings*

Introduction

A wide range of disasters, such as hurricanes, earthquakes, and wildfires threaten the resilience of communities around the world. It has been observed that the frequency of such disasters has increased during recent decades (Aghababaei et al. 2018; NOAA 2020). A great number of studies have focused on a better understanding of hazard loads, their direct and indirect impacts, the restoration of communities in the aftermath, and ways to improve the resilience of communities against these events (Aghababaei et al. 2020; Aghababaei and Mahsuli 2018, 2019; Attary et al. 2019; Cornell and Krawinkler 2000; Koliou et al. 2018; Koliou and van de Lindt 2020; Lounis and McAllister 2016; Memari et al. 2018; Zhang et al. 2018). One of the key elements for conducting all of the aforementioned studies is having relevant data. These data can be collected from various resources, spanning from experimental studies to post-disaster field surveys, depending on the objective of each study. In most cases, such data are accessible for a limited amount of time, and vanish rapidly as the community starts to recover. Additionally, full-scale experiments are very costly and need access to unique facilities, and hence, it is of great importance to collect a comprehensive dataset during and after every full-scale test using a variety of instruments.

Conventionally, observations from full-scale shake table experiments are collected using traditional instruments, and the damage is recorded using a combination of note taking and ordinary cameras. In contrast, other similar fields of study have adopted advanced data collection techniques, such as post-disaster data collection in the aftermath of hurricanes, earthquakes, among others. One common modern surveying technique used in post-disaster reconnaissance studies is Light Detection and Ranging (LiDAR) scanning, which has been used widely. The next section of this paper discusses previous work and advancements in the use of LiDAR scanning for time-sensitive data collection.

Literature Review and Research Gaps

To collect time-sensitive data (either during reconnaissance or lab-controlled experimental studies), different forms of survey and instrumentation have been evaluated in the literature, including direct field inspections as well as modern and traditional instrumentation. For example, to collect damage data after natural disasters, field inspections (Aghababaei et al. 2018; van de Lindt et al. 2007), geospatial videos (Curtis and Fagan 2013; Mills et al. 2010), Unmanned Aerial Vehicle (UAV) images (Pinelli et al. 2018), as well as LiDAR scanning (Barbosa et al. 2017; Brando et al. 2017; Zhou et al. 2019) have been employed. Furthermore, to collect time-sensitive data from lab-controlled experimental studies, various methods including a combination of traditional instrumentation (e.g., accelerometers, displacement transducers, etc.) and visual damage inspections (Filiatrault et al. 2010; van de Lindt et al. 2011, 2012), LiDAR scanning (Kashani and Graettinger 2015; Olsen et al. 2010), and digital image correlation (Kramer et al. 2016) were utilized. Each method of data collection has been selected depending on the scope of the study and the method’s advantages and disadvantages. Recently, various studies have integrated modern technologies, such as remote sensing techniques (Olsen et al. 2010; Soti et al. 2020; Zhou et al. 2019), with the data collection efforts as an alternative to traditional reconnaissance field surveys.

With regard to LiDAR, a number of studies employed LiDAR point clouds to comprehensively collect 3D data to identify and quantify the damage of the inspected infrastructure. Olsen and Kayen (2013) discussed special considerations when performing LiDAR scanning in post-disaster environments, with respect to procedures during planning, field reconnaissance, collaboration, data acquisition, processing, and analysis. Yu et al. (2017) utilized LiDAR scans to collect damage data from an 18-story building located in Nepal damaged by the 2015 Gorkha earthquake and its aftershocks; these researchers identified and quantified damage in two key building components (coupling beams and infill walls) in different stories using the collected scans. The results presented by Yu et al. (2017) indicate a good correlation with the damage states predicted by the finite element model of the building subject to the recorded earthquakes. A number of studies also used LiDAR data to detect roof damage after severe weather events (Kashani et al. 2016; Kashani and Graettinger 2015). More specifically, Kashani and Graettinger (2015) developed a clustering-based method to automatically detect roof damage using LiDAR data collected after disasters. To develop their algorithm settings, they conducted multiple experiments under controlled conditions inside a laboratory and trained their algorithm using the collected LiDAR data. Olsen et al. (2010) and Kashani and Graettinger (2015) are amongst the few lab-controlled studies utilizing LiDAR scanning instruments to detect damage.

Despite the aforementioned advancements in collecting time-sensitive data in other related research fields, to the best knowledge of the authors of the current paper, there is no prior full-scale shake table experimental study in the literature utilizing LiDAR scanning to collect and detect damage. The current study targeted to further demonstrate the feasibility, capabilities, and importance of using such LiDAR scanning survey techniques in full-scale shake table experiments, as well as their advantages and challenges when applied to such experimental programs.

Advantages, Disadvantages, and Limitations

According to the results of this study, there are advantages, disadvantages, and limitations for using LiDAR scanning to collect time-sensitive data of full-scale shake table tests. The main advantages are as follows:

(i) The resulting point cloud is comprehensive; it encompasses the observations of all interior and exterior components of the building specimen, its content, and its surrounding in a single dense point cloud.

(ii) Observations and measurements can be taken after the test specimen is demolished; this significant feature of the resulting point cloud enables researchers, even those not present at the time of the experiment, to observe the results, inspect the building, conduct measurements and perform further analyses.

(iii) Using the resulting point cloud, the user can create virtual walkthroughs in the interior and exterior of the test specimen to mimic physical inspections on the shake table between tests. Appropriate computer programs are used to move around and inside the point cloud of the building, zoom in and out, and safely perform detailed measurements for the desired purpose.

(iv) Various types of analyses can be conducted using the point clouds in addition to simple measurements. As discussed previously, studies in the literature employed methods to automatically detect damage, and most importantly, *quantify* its extent (Kashani and Graettinger 2015; Yu et al. 2017).

There are also disadvantages and limitations in using LiDAR scanning for data collection from full-scale shake table tests. They are listed as follows:

(i) LiDAR scanning provides no information about the time history response of the building during shaking; rather, it preserves the state of the building before and after each test. Although this is sufficient to collect permanent deformations of the specimen and the damage incurred, it lacks the time history response of the building.

(ii) There are tradeoffs and potential limitations that should be considered with respect to the accuracy of LiDAR scanners. It is worth noting that there are two components to the LiDAR scanners used in this study; one is related to the scanning (point measurements) and the other to imaging (digital photographs). The images allow for the color/pixelization of the point cloud data but are also crucial for damage identification. Scanners are extremely useful to capture objects in the scene, while efficiently and accurately capturing deformations. However, for crack detection and crack width quantification, there is a need to balance the resolution in terms of the point measurement scanning accuracy and the number of pixels of the images or the need to do localized scans, which require knowledge of the locations of the cracks. The balance depends not only on the characteristics of the scanner, but also how they are used and their setup with respect to the objects of interest. For example, in the current study, the scanners used were capable of producing higher resolution scans and images, but at an increased cost in terms of the time taken per scan, which was not compatible with the fast pace of shake-table testing program. As a consequence, there may be limitations in the ability of scanners to collect damage data in an expedited way, especially when collecting data needed to quantify crack locations and widths. In addition, development of algorithms for automatic damage detection are needed since only a few examples are available in the literature for use in structural engineering applications (Soti et al. 2020; Wood et al. 2017).

In the following sections, first the scope and objectives of this study are summarized. Second, details of the test specimens as well as the traditional and LiDAR equipment used in this study are presented. Third, the LiDAR scanning procedures adopted are described, and details of the scanning for each phase of the tests are provided. A formalized LiDAR scanning procedure is proposed based on lessons learned during damage assessments. The paper continues with comparison of the damage assessments through visual inspection and LiDAR scans by illustrating various examples of structural and nonstructural components. Thereafter, automatic damage detection using LiDAR point clouds by point-to-point comparison is discussed; an example of automatic damage detection on the eastern wall of Building A on the last test day is presented. Finally, the various types of information acquired using traditional and LiDAR scanning, their complementary role in comprehensive data collection, and the potential of using modern survey techniques in full-scale shake table experiments are discussed.

Objectives and Scope

The current study aimed to advance the use of damage surveying techniques for full-scale shake table tests using LiDAR scanning as an alternative to traditional techniques or as a complementary survey tool. For this purpose, the current study utilized LiDAR scanning to collect as-built geometry of the building specimens as well as damage data of a set of full-scale shake table tests conducted on two wood residential buildings. The tests were conducted in the E-Defense facility in Miki, Japan, as a part of the first stage of a five-year project titled "Tokyo Metropolitan Resilience Project". The objectives of this study are to:

(i) Propose a formalized survey procedure for utilizing LiDAR scanning techniques in full-scale shake table tests, based on lessons learned during this project.

(ii) Present various showcases of measurements conducted and damage detected on structural and nonstructural components as examples of the capabilities of the resulting LiDAR data (containing point clouds and photographs taken by scanner), and compare them with photographs taken by ordinary cameras.

(iii) Evaluate the accuracy of the measurements, compare them with the results of traditional measurement instruments, and identify the advantages and drawbacks of using LiDAR for full-scale shake table experiments.

Test Specimens Description

The five-year project discussed in this paper, the "Tokyo Metropolitan Resilience Project", is currently in progress in Japan to assess the resilience of the Tokyo urban area (Nagae et al. 2020b). During the first stage of this project, a series of shake table studies on two full-scale wood residential 161.5 m^2 (1738 ft^2) buildings with different structural systems and foundation conditions were conducted at the E-Defense facility. Figure 1 presents photographs from the four corners of the two buildings prior to testing on the shake table. These two three-story buildings represent the trend of construction in densely populated urban areas in Japan (Nagae et al. 2020b). The designs correspond to "Grade-3 construction" according to current Japanese design guidelines (Nagae et al. 2020a). Figure 2 presents the elevation views of the first building, called herein "Building A". The first and second story were 2.775 m (9.1 ft) tall while the third story was 2.769 m (9.08 ft) tall. Plan views of all three floor levels are shown in Figure 3. A kitchen and dining room were located in the first story along with a laundry room and a full bathroom. Three bedrooms were located in the second story and a master bedroom was located in the third story. Additionally, a large living room area was located on the third story of the building. The second building, called herein "Building B", was identical to Building A architecturally, except for its windows. To avoid repetition, the plan and elevation views of Building B are not presented since the differences are very minor compared to Building A.

Building A was constructed using the post-and-beam method. The building had let-in X-braces in both horizontal directions, which were fixed using metal connectors. Figure 4 presents the post-and-beam structure of Building A, where labels in this figure correspond to the grid labels in Figure

3. Structural plywood for the exterior walls was attached using nails. This building was initially located on a seismic base-isolation system (test days 1 and 2), but was fixed for test days 3 and 4.

Building B was constructed using shear walls. The panels were prefabricated and were composed of vertical and lateral frame elements and shear wall panels that were fixed to sills using nails and metal framing anchors. The design of Building B was similar to typical US wood building designs and construction using wood structural panel shear walls with framing members and blocking, except that in the US larger framing members are used at adjoining panel edges for multiple rows of nails and larger-diameter nails provide for higher strength shear walls (American Wood Council 2015; 2018). In addition, in the US construction, design for shear and overturning provides for properly sized tension and compression chords as well as shear and overturning anchorage. Building B was initially placed on a concrete mat foundation constructed on compacted soil that was contained in a reinforced concrete open-top box, simply referred to as soil box hereafter. Note that the small volume of soil included in this test could not properly represent wave propagation, ground motion attenuation, and radiation damping patterns below the foundation. The foundation conditions were modified for the latter part of the test program.

Instrumentation

This section presents LiDAR scanning data collected in this study, the main features of the equipment used, as well as a summary of traditional instruments utilized and their location.

Three LiDAR scanners were used including: (i) two close-range LiDAR scanners (Figure 5a) with an accuracy of 4 mm in 10 meters distance and a scanning distance range of 60 meters, which were used to scan the interior of the buildings, and (ii) a long-range LiDAR scanner (Figure 5b) with an accuracy of 4 mm and a scanning distance range of 1,200 meters, which was suitable for scanning building exteriors. Exterior scans were generally captured from three observation decks around the shake table as indicated in Figure 1, and hence, the close-range scanners could not be utilized for this purpose. In addition to the LiDAR scanners, in order to assemble the scans more efficiently and precisely during post-processing, one total station (Leica Nova TS16I) was utilized to collect the coordinates of multiple targets located around the buildings and on fixed points on the walls of the laboratory.

Various types of traditional instruments including triaxial accelerometers, strain gages, and Linear Variable Displacement Transducers (LVDTs) were utilized to measure the responses of the buildings subjected to various shaking intensities during the four days of testing. The traditional instruments used by the authors' team are listed in Table 1, and the accelerometer locations for both buildings are shown in Figure 6. Although not shown in Figure 6, Building B instrumentation also included triaxial accelerometers, one on the soil box and one on the piping inside the soil, and four LVDTs, one at each corner of the building on the soil box in the vertical direction.

Test Sequence and Lidar Scanning Procedure

Table 2 presents the shaking trials on each test day along with the earthquake intensities and base condition. It should be noted that a white noise test was conducted before and after each trial to evaluate the modal features (e.g., frequency, damping, and mode shapes).

Experiments started on test day 1 with Building A on a seismic base-isolation system and Building B on a foundation constructed in a soil box by applying JMA 25%, JMA 50%, JR 25%, and JR 50% motions (JMA Kobe and JR Takatori are two recorded motions for the 1995 Kobe earthquake in Japan). Acceleration histories record and acceleration response spectra of JMA 100% and JR 100% records are presented in Figure 7 and Figure 8, respectively. On test day 2, the buildings were subjected to 100% JMA and 100% JR. On test day 3, Building A was fixed and Building B was still on the soil box but with twenty cast iron plates inserted between the foundation slab and soil to reduce frictional resistance of the foundation slab (Nagae et al. 2020a). The two buildings were subjected to JMA 25%, JMA 50%, JMA 100%, and JR 100%. On test day 4 (the final test day), both buildings were fixed on the shake table and subjected to the JMA 100% motion only. Plans to apply JR 100% per the excitation schedule were cancelled due to severe damage to Building B during the JMA 100% motion.

Table 3 details the scanning sets obtained before, during, and after each test day. This table summarizes the experiment stage of each scanning set operated, whether it included the building interiors, exteriors, or both, and the number of stations (i.e., setups) where scans were conducted for each set. The first two rows of this table represent the pre-test scans conducted for reference and comparison prior to the buildings incurring any damage. One phase of pre-test scanning was conducted using a close-range scanner on both the interior and exterior while the buildings were located outside the laboratory, toward the end of construction and prior to installing furniture.

Additional pre-test scans were acquired using both close-range and long-range scanners for the interior and exterior, respectively, after the buildings were moved to the shake table. The second set of pre-test scans provided a benchmark point cloud of the buildings on the shake table and after the furniture was placed inside the buildings.

During the experiments, LiDAR scans of both the interior and exterior of the buildings were taken at the beginning and end of each test day, in addition to exterior scans in-between shake-table when the tight testing schedule allowed. The in-between scans were performed from the observation deck using only the long-range LiDAR scanner during the visual inspection timeframe in-between tests.

Various challenges were faced when conducting the LiDAR scanning during the experiments as well as during the post-processing stage to assemble the scans together. Consequently, a scanning procedure to collect LiDAR data is proposed for use in future shake table testing, as illustrated in Figure 9. The procedure includes guidelines for performing the scans and post-processing more efficiently according to the lessons learned in this study. These guidelines are:

i. Before going to the laboratory: Prepare a scanning plan according to the available time for conducting the survey in an efficient and timely manner. This plan should specify the location of scanning stations and assign a corresponding number to each station in order to assemble these scans easier during the data processing stage. The location of stations and their distance are determined based on the testing schedule, the number of available scanners and team members to operate them, and the assigned scanning time. Some scanning stations should be located in the joints connecting the interior and exterior of the building at a closer distance if possible; it is challenging to assemble interior and exterior scans without scans in the joints during registration of the point clouds.

ii. Pre-test preparations in the laboratory: Place numbered targets inside and outside the building before scanning, which is crucial to assemble scans in a much more efficient manner during the data processing stage. Scanning acquisitions from stations inside and outside the buildings are registered together using their mutual features to form a 3D point cloud of the complete building. A drawing of the targets indicating their location and number should be prepared for future reference to easily locate the scans by inspection into the drawing, and subsequently, assemble them faster. A number of commercial software packages utilized to register the scans have the ability to assemble scans that include mutual targets automatically, which notably helps speed up the registration process. In addition, even if the software does not automatically identify mutual targets to assemble the scans, the scans can be assembled by manually inspecting and locating the common targets. As an illustration of the relative location of the scanning setups and target positions, Figure 10 presents the locations of targets and scanning setups in each story for test day 3.

iii. <u>Technical preparations prior to each scanning day</u>: This step is crucial to avoid delays on the scanning day. Given the variety of devices used in these types of surveys (e.g., close- and long-range LiDAR scanners, tablets, cameras, total station, walkie-talkies, etc.) each of them should be prepared and tested prior to the operation day. Charge all batteries fully for each device the day before scanning since these batteries usually discharge after a certain amount of time. Check the available memory of each device to ensure sufficient space for the operation. To avoid disruptions on the scanning day, back-up instruments are advisable in case of any malfunction. This includes extra batteries, memory, and survey instruments (if available).

iv. <u>During each scanning day</u>: On the scanning day, divide the instruments among team members based on the number of personnel required to operate each instrument. To operate LiDAR scanners, two persons are needed to operate a long-range scanner and one person (preferably two if possible) is needed to operate a close-range scanner. Initiate scans from the first marked station and continue in accordance with the scanning plan and sequence. Monitor each scanner and prevent others from moving the scanner or blocking its surroundings. In addition, change the batteries of scanners during the scanning day on a pre-determined schedule to avoid disruptions and incomplete scans.

v. <u>After each scanning day</u>: Transfer the scans acquired immediately into external hard drives, computers, and internet storages, and create backups. This is crucial for preserving and creating redundancy of survey data, especially when there is more than one day of scanning. In addition, document the data effectively by arranging scan files with appropriate names describing the date and phase of the test as well as the location of the stations.

Damage Assessments through Visual Inspection and LiDAR Scans

In this section, various examples of structural and nonstructural damage are presented through visual inspections performed using ordinary cameras as well as post-processed collected LiDAR data. The capabilities of LiDAR scans to detect and quantify damage are presented and discussed in this section. After the registration and post-processing steps, the separately collected LiDAR scan data was used to develop a 3D immersed view of the buildings through a massive point cloud. As an illustration, a screenshot of the 3D view of post-processed registered LiDAR data for test day 2 is presented in Figure 11, which was developed from data for both the interior and exterior scans registered together. One can move around and inside the buildings in the resulting 3D point cloud for various purposes, such as identifying damage, performing measurements, automatically detecting damage, etc. This section continues with examples of structural and nonstructural damage detected through visual inspection and virtual inspections of LiDAR point clouds. Afterwards, as an application of LiDAR point cloud data, instants for the pre-test undamaged state and post-test damage state point clouds are compared through cloud-to-cloud comparison to automatically detect damaged locations.

Structural Damage

During the first two days of testing, there was no observable structural damage, and hence, neither the cameras nor the LiDAR scanners detected and recorded any structural damage. During test day 3, damage to the structural systems of both buildings was identified, but structural elements were not exposed, so damage could not be easily observed. However, in test day 4, major damage occurred in both buildings, and hence, damaged structural elements were exposed due to spalling of the façade, wallboards, and gypsum wallboards on the interior. Damage was observable from photographs taken by cameras as well as the LiDAR scans. As an example, a distorted column in Building B is depicted with a photograph taken by a camera (Figure 12a) as well as a close-up view screenshot of the LiDAR point cloud data (Figure 12b). Similarly, Figure 13 illustrates the structural damage of two elements of ruptured wood bracing on the east and west sides of Building A through photographs and screenshots of the point clouds. The damaged wood bracing on the east side (Figure 13a and b) was exposed because the façade wallboards spalled off the surface, and as a result, both ordinary cameras and LiDAR scanners captured it. Similarly, the damaged wood bracing on the west side (Figure 13c and d) was exposed since the gypsum wallboards spalled off the interior perimeter walls, and the damage was apparent from visual inspections and LiDAR scans. Figure 13b presents a side view of the damaged wood bracing of Figure 13a, from which the out-of-plane buckling of the bracing elements relative to the wall surface was measured, as presented by a color map. The measurement indicates that the wood bracing buckled out-of-plane approximately 0.217 m (0.696 ft) at its ruptured location. Figure 13d illustrates the use of LiDAR scan data to capture high-quality point clouds of the damaged components in three dimensions, while the photographs taken using high-quality cameras (Figure 13c) only provide two-dimensional representations of the damage. Thus, the point cloud data can be used to observe, assess, and conduct quantitative and qualitative measurements virtually from multiple points of view after the experiments have occurred. A number of measurements (such as the distance from the rupture point to the ends of the braces, the dimensions of the bracing elements, etc.) are marked on this point cloud to illustrate how various measurements are obtained using LiDAR point clouds.

Nonstructural Damage

Visible damage to the building facades was observed during the last two days of testing. Figure 14 and Figure 15 present photographs taken from the east and west sides of Buildings A and B on test day 3 and 4, respectively, along with photographs of the damage detected through post-processed LiDAR point clouds. Because of the short distance between the two buildings the façades on the adjacent sides (i.e., Building A west side and Building B east side) were not easily accessible compared to the other two sides, and hence, neither the camera photographs nor the LiDAR scans produced quality acquisitions, as Figure 14b and Figure 15b and 15c also indicate. However, by increasing the number of scans in the region between the buildings and setting scanning stations to maximize the coverage of the walls, it was possible to enhance the quality of the point clouds which should be considered in future studies.

Tables 4 and 5 list the measurements for locations of detected damage as labeled in Figure 14 and Figure 15 for test days 3 and 4, respectively. Three types of damage are reported for the façades: cracks, spalling of the plasterboards, and façade damage caused by distortion of an exterior column in Building B. The measurements include crack lengths, areas of spalled sections, and the rotation angle relative to vertical of the distorted column. As mentioned earlier in this paper, cracks were detected and quantified using LiDAR data, which contains both point clouds and pictures taken during the scanning. A good resolution of both components of LiDAR data (i.e., point measurements and color—pixelized) was required for this purpose. To detect damage, the point clouds were viewed from a zoomed-in perspective to inspect each part from a closer view and to distinguish cracks from the shades that are visible in these figures. In addition, panoramic photographs taken by scanners at each scanning station were used to locate visual damage faster and to distinguish between damaged parts and shades. Damage incurred in the buildings was considerably more severe on test day 4 (Figure 15) compared to test day 3 (Figure 14). This damage is readily observed through the camera photographs and from the point clouds. Any type of measurement on the point clouds can be taken to evaluate the extent of the damage, and measurements provided here are just representative examples to illustrate the utility of the resulting point clouds for conducting damage assessments any time after the tests have occurred.

Damage to interior walls varied from minor cracks to spalling of gypsum wallboards and buckling of wood studs. A large number of photographs were taken during inspections in order to record the damage of multiple walls in all three stories of each building. LiDAR scans after each test day efficiently captured the damage incurred by partition walls. Figure 16 presents a screenshot of the point clouds of Building A's east side interior walls after test day 3. In order to observe, inspect, and compare the damage on all east side interior walls of Building A simultaneously, their point clouds were easily cut out of the total point clouds of the two buildings (Figure 11). Compared to visual inspection or camera photographs, LiDAR point clouds uniquely enable the user to easily access and inspect any damaged component, compare similar components simultaneously, and conduct measurements after removal of the specimen from the testing facility. For example, Figure 16 shows that damage to the interior wall surfaces is most severe in the first story, while the least damage occurs in the third story. Users of LiDAR point clouds can zoom in, rotate, and translate these clouds to better observe or measure the extent of damage. To better illustrate, sections A and B of Figure 16 are shown in Figure 17 in a close-up view that was generated by zooming in to the point cloud. Damage states, including cracks and gypsum wallboard spalling, are marked with measurements of the crack length. The LiDAR scanner employed in the current study did not capture hairline cracks on the partition walls, but higher accuracy scanners might be utilized.

Damage Detection by Point-to-Point Comparison

In addition to the measurements performed manually using LiDAR scans, damage was detected automatically by comparing the scans acquired after each test day to the reference scans acquired prior to the start of testing (see scanning schedule in Table 3). For this purpose, a feature called *"cloud to cloud compared"* was utilized to compare point clouds of the damaged and reference undamaged buildings. As an example, a cloud-to-cloud comparison of the exterior plasterboard façade is presented in Figure 18. To process the point clouds for comparison, the east side wall of Building A was cut out of the pre-test scans and test day 4 scans individually, and these scans were cleaned up to eliminate disruptions caused by noise. In addition, windows were deleted from the cloud to prevent false damage detection caused by reflected points. Afterwards, the scans were aligned on top of each other with minor deviation, and the out-of-plane point-to-point distance between the two clouds was computed over the wall area. Figure 18 shows the distance distributions throughout the selected wall; distances below 0.005 meters are white, while distances exceeding 0.005 meters – indicating damage – appear in color according to the colorbar.

Comparison of Traditional and LiDAR Scanning Instrumentation

Since LiDAR scans are acquired after each test, they represent a snapshot of the status of the building after the test is finished, not the whole time-history of the building movement and damage during the shaking. Hence, the permanent displacements of the building and its components can be measured using LiDAR point clouds, but the displacement time history during shaking cannot be measured. As a result, the measurements conducted from point clouds can only be compared to the final values in the time history of the building displacement.

As an example, during test day 2, Building B moved (translated and rotated) relative to the soil box during intense shaking (for JMA 100%). Figure 19 presents the recorded input motion on the shake table (for JMA 100%), and the low-pass filtered (30 Hz) displacement history of each corner of Building B relative to the soil box, which was recorded in the x and y direction by laser meters. The measurements at the end of the test (i.e., the permanent displacements) are marked by a red circle in Figure 19. In Figure 20, screenshots of the point clouds before and after the test are presented by red and white colors. For this purpose, the portion of the LiDAR point cloud at the base level (where laser meters were installed) was cut out of the total point clouds acquired both before and after the JMA 100% shake table test. The measurements in all four corners were obtained by computing the distance between the corners of the two point clouds, which indicates the movement of each corner after shaking compared to before shaking. In Figure 20, displacement values from traditional laser meters are reported in green and those from LiDAR point clouds are reported in yellow. As shown in Figure 20, permanent displacements derived from traditional and LiDAR scanners are very consistent except for the x direction of the southwest corner. Examination of the time history of the x-direction movement of this corner (Figure 19c) suggests a malfunction in the performance of the laser meter, which caused it to report the exact same number (507.588 mm) after a jump in its measurement at 17.69 seconds while other laser meters still reflected small oscillations in their time histories. This malfunction could be attributed to an error in the laser meter, local failure/deformation, or damage to the laser meter or its anchorage.

These examples have illustrated the capabilities of LiDAR point clouds to be a complementary source of information to traditional instruments during full-scale shake table experiments. Traditional instruments collect the response time history of the building and its components, such as accelerations, displacements, and loads, while LiDAR scanners collect a comprehensive point cloud of the specimen final response containing the permanent displacements as well as detailed damage information of the components of the specimen. While these two survey methods are complementary, they have overlaps as well, such as the example presented in Figure 20 that compared the permanent displacements. Furthermore, recently, methodologies are developed in the literature to optimize the number and location of traditional instruments (Roohi et al. 2019; Roohi and Hernandez 2020). As illustrated, when a traditional instrument records an erroneous measurement, it can be corrected using the LiDAR data. Other examples of permanent displacements that could be measured using LiDAR point clouds include movement of contents inside the specimen, and out-of-plane displacements of walls, facades, and other surfaces. The latter type of measurements are very challenging using traditional survey techniques, while out-of-plane displacement can be easily measured by comparing LiDAR point clouds before and after the test, similar to the automatic damage detection performed in Figure 18.

Summary and Conclusions

This study has focused on the use of LiDAR scanning techniques to collect time-sensitive data during full-scale shake table experiments of buildings. Two full-scale three-story wood residential houses, typical of densely populated urban areas, were tested on the largest shake table in the world at the E-Defense facility in Miki, Japan, as the first stage of a five-year project studying the resilience of metropolitan areas in Japan. The current study utilized LiDAR scanners to collect time-sensitive information during these experiments, and a systematic procedure for using modern survey techniques has been developed based on the lessons learned. The two buildings in this study were identical from the exterior but had notably different structural details. Information about their structural and nonstructural details has been provided, along with their base condition on each test day, and shaking intensity in each testing phase. Damage assessment through visual inspection, as conventionally employed following full-scale shake table tests, was compared to assessments performed using LiDAR point clouds. For this purpose, various examples assessing damage of structural and nonstructural components through both visual inspection and LiDAR point clouds were illustrated. These examples have led to the following conclusions:

As a key advantage, LiDAR point clouds have the ability to measure the extent of damage (e.g., crack length) with a high level of accuracy even after the specimens have been removed from the test facility and demolished. Damaged areas or components of the building can be automatically detected by comparing the point clouds collected before and after a shake. This automatic damage detection feature was demonstrated using point clouds on the façade surface of one of the buildings obtained before and after shaking. Finally, LiDAR measurements can be used to complement or validate permanent measurements taken from traditional instruments in addition to their comprehensive damage data collection. Since LiDAR point clouds are collected after the shaking is performed, their measurements are only comparable to the residual/permanent displacements of the buildings and their components, and cannot capture the whole response time history. On the second test day, the building on the soil box experienced a permanent movement that was measured through eight laser meters at the corners of the building. These measurements were validated with acceptable accuracy through measurements performed using LiDAR point clouds acquired before and after the shaking. Furthermore, a discrepancy in the results of one of the laser meters was conclusively attributed to an erroneous measurement of the laser meter based on the comprehensive and consistent information obtained by the LiDAR point clouds.

This study concludes that collecting data from full-scale shake table experiments using LiDAR scanners in conjunction with response acquisition instruments (e.g., accelerometers, etc.) results in a comprehensive damage and response dataset, which enables researchers to conduct further analyses and measurements on the test specimens after the tests are completed or even after the specimens are demolished. This is crucial since full-scale shake table tests are costly and need unique facilities to be carried out. To accomplish this, traditional instruments collect the response time history of different parts of the building at discrete locations (e.g., acceleration and displacement) effectively, while LiDAR scans collect the damage observations in a comprehensive and accurate way. In addition to the damage data, LiDAR point clouds provide accurate information about permanent changes after the shaking, such as permanent/residual displacements, out-of-plane displacement of the walls and surfaces, and movement of the contents inside the building.

Data Availability Statement

Some or all data, models, or code that support the findings of this study are available from the corresponding author upon reasonable request.

Acknowledgements

This study is funded by the US National Science Foundation (NSF) under Award No. CMMI 1829433 and 1829412. This financial support is greatly appreciated. Data was collected in part using equipment provided by the NSF as part of the RAPID Facility, a component of the NHERI under Award No. CMMI 1611820. Any opinions, findings, conclusions, and recommendations presented in this paper are those of the authors and do not necessarily reflect the views of NSF. The authors would also like to acknowledge the Japanese team led by Prof. Takuya Nagae for their collaboration and support during the testing phase.

References

Aghababaei, M., Koliou, M., Pilkington, S., Mahmoud, H.M., van de Lindt, J.W., Curtis, A., Smith, S., Ajayakumar, J. and Watson, M. (2020). "Validation of Time-Dependent Repair Recovery of the

Building Stock following the 2011 Joplin Tornado." *Natural Hazards Review* (Special Issue/Collection on "Enabling Resilient and Sustainable Communities"), American Society of Civil Engineers, 21(4), 10.1061/(ASCE)NH.1527-6996.0000408.

Aghababaei, M., Koliou, M., and Paal, S. G. (2018). "Performance Assessment of Building Infrastructure Impacted by the 2017 Hurricane Harvey in the Port Aransas Region." *Journal of Performance of Constructed Facilities*, 32(5), 04018069.

Aghababaei, M., Koliou, M., Watson, M., and Xiao, Y. (2020). "Quantifying post-disaster business recovery through Bayesian methods." *Structure and Infrastructure Engineering*, 1-19.

Aghababaei, M., and Mahsuli, M. (2018). "Detailed Seismic Risk Analysis of Buildings Using Structural Reliability Methods." *Probabilistic Engineering Mechanics*, 53, 23–38.

Aghababaei, M., and Mahsuli, M. (2019). "Component damage models for detailed seismic risk analysis using structural reliability methods." *Structural Safety*, 76, pp.108-122.

American Wood Council (2015). "Special Design Provisions for Wind and Seismic." *SDPWS-2015*, Leesburg, VA.

American Wood Council 2018. "National Design Specifications (NDS) for Wood Construction." *ANSI/AWC NDS-2018*, Leesburg, VA.

Attary, N., van de Lindt, J. W., Mahmoud, H., and Smith, S. (2019). "Hindcasting Community-Level Damage to the Interdependent Buildings and Electric Power Network after the 2011 Joplin, Missouri, Tornado." *Natural Hazards Review*, American Society of Civil Engineers, 20(1), p.04018027.

Barbosa, A. R., Fahnestock, L. A., Fick, D. R., Gautam, D., Soti, R., Wood, R., Moaveni, B., Stavridis, A., Olsen, M. J., and Rodrigues, H. (2017). "Performance of medium-to-high rise reinforced concrete frame buildings with masonry infill in the 2015 Gorkha, Nepal, earthquake." *Earthquake Spectra*, SAGE Publications Sage UK: London, England, 33(1_suppl), 197–218.

Brando, G., Rapone, D., Spacone, E., O'Banion, M. S., Olsen, M. J., Barbosa, A. R., Faggella, M., Gigliotti, R., Liberatore, D., and Russo, S. (2017). "Damage reconnaissance of unreinforced masonry bearing wall buildings after the 2015 Gorkha, Nepal, Earthquake." *Earthquake Spectra*, SAGE Publications Sage UK: London, England, 33(1_suppl), 243–273.

Cornell, C. A., and Krawinkler, H. (2000). "Progress and challenges in seismic performance assessment." *PEER Center News*, 3(2), 1–4.

Curtis, A., and Fagan, W. F. (2013). "Capturing damage assessment with a spatial video: An example of a building and street-scale analysis of tornado-related mortality in Joplin, Missouri, 2011." *Annals of the Association of American Geographers*, Taylor & Francis, 103(6), 1522–1538.

Filiatrault, A., Christovasilis, I. P., Wanitkorkul, A., and van de Lindt, J. W. (2010). "Experimental Seismic Response of a Full-Scale Light-Frame Wood Building." *Journal of Structural Engineering*, American Society of Civil Engineers, 136(3), 246–254.

Kashani, A. G., and Graettinger, A. J. (2015). "Cluster-Based Roof Covering Damage Detection in Ground-Based Lidar Data." *Automation in Construction*, Elsevier B.V., 58, 19–27.

Kashani, A. G., Graettinger, A. J., and Dao, T. (2016). "Lidar-Based Methodology to Evaluate Fragility Models for Tornado-Induced Roof Damage." *Natural Hazards Review*, American Society of Civil Engineers, 17(3), 1–9.

Koliou, M., and van de Lindt, J. W. (2020). "Development of Building Restoration Functions for use in Community Recovery Planning to Tornadoes." *Natural Hazards Review*, American Society of Civil Engineers, 21(2), 04020004.

Koliou, M., van de Lindt, J. W., McAllister, T. P., Ellingwood, B. R., Dillard, M., and Cutler, H. (2018). "State of the research in community resilience: progress and challenges." *Sustainable and Resilient Infrastructure*, Taylor & Francis, 9689, 1–21.

Kramer, A., Barbosa, A. R., and Sinha, A. (2016). "Performance of steel energy dissipators connected to cross-laminated timber wall panels subjected to tension and cyclic loading." *Journal of Structural Engineering*, American Society of Civil Engineers, 142(4), E4015013.

van de Lindt, J. W., Gupta, R., Pei, S., Tachibana, K., Araki, Y., Rammer, D., and Isoda, H. (2012). "Damage assessment of a full-scale six-story wood-frame building following triaxial shake table tests." *Journal of performance of constructed facilities*, American Society of Civil Engineers, 26(1), 17–25.

van de Lindt, J. W., Pryor, S. E., and Pei, S. (2011). "Shake table testing of a full-scale seven-story steel-wood apartment building." *Engineering Structures*, Elsevier Ltd, 33(3), 757–766.

Lounis, Z., and McAllister, T. P. (2016). "Risk-Based Decision Making for Sustainable and Resilient Infrastructure Systems." *Journal of Structural Engineering*, American Society of Civil Engineers, 142(9), F4016005.

Memari, M., Ameri, M. R., Pilkington, S. F., Mahmoud, H., Attary, N., van de Lindt, J. W., and Masoomi, H. (2018). "Minimal Building Fragility Portfolio for Damage Assessment of Communities Subjected to Tornadoes." *Journal of Structural Engineering*, American Society of Civil Engineers, 144(7), 04018072.

Mills, J. W., Curtis, A., Kennedy, B., Kennedy, S. W., and Edwards, J. D. (2010). "Geospatial video for field data collection." *Applied Geography*, Elsevier, 30(4), 533–547.

Nagae, T., Uwadan, S., Takaya, K., Yenigodan, C., Yamada, S., Kashiwa, H., Hayashi, K., Takahashi, T., and Inoue, T. (2020a). "Sliding-Rocking Combined Actions at Base Foundation Influencing Global and Local Deformations of Upper Wood Structure" *17th World Conference on Earthquake Engineering*, 17WCEE, Sendai, Japan.

Nagae, T., Uwadan, S., Yenigodan, C., Yamada, S., Kashiwa, H., Hayashi, K., Takahashi, T., and Inoue, T. (2020b). "The 2019 Full-Scale Shake Table Test Program of Wood Dwellings, *17th World Conference on Earthquake Engineering*, 17WCEE, Sendai, Japan.

NOAA (National Oceanic and Atmospheric Administration). 2020. "Billion-dollar weather and climate disasters: Time series." Accessed June 21, 2020. https://www.ncdc.noaa.gov/billions/time-series.

Olsen, M. J., Kuester, F., Chang, B. J., and Hutchinson, T. C. (2010). "Terrestrial laser scanning-based structural damage assessment." *Journal of Computing in Civil Engineering*, American Society of Civil Engineers, 24(3), 264–272.

Pinelli, J.-P., Roueche, D., Kijewski-Correa, T., Plaz, F., Prevatt, D., Zisis, I., Elawady, A., Haan, F., Pei, S., Gurley, K., Rasouli, A., Refan, M., Rhode-Barbarigos, L., and Moravej, M. (2018). "Overview of damage observed in regional construction during the passage of Hurricane Irma over the state of Florida." Proc., ASCE Forensic, 18.

Roohi, M.; Hernandez, E.M. Performance-based Post-earthquake Decision-making for Instrumented Buildings. arXiv 2020, arXiv:2002.11702.

Roohi, M., Hernandez, E. M., & Rosowsky, D. (2019). "Nonlinear seismic response reconstruction and performance assessment of instrumented wood- frame buildings—Validation using NEESWood Capstone full- scale tests." *Structural Control and Health Monitoring*, 26(9), e2373.

Soti, R., Abdulrahman, L., Barbosa, A. R., Wood, R. L., Mohammadi, M. E., and Olsen, M. J. (2020). "Case study: Post-earthquake model updating of a heritage pagoda masonry temple using AEM and FEM." *Engineering Structures*, Elsevier, 206, 109950.

Wood, R.L., Mohammadi, M.E., Barbosa, A.R., Soti, R., Abdulrahman, L., Kawan, C.K., Shakya, M., Olsen, M.J. (2017). "Damage Assessment and Modeling of the Five Tiered Pagoda Style Nyatapola Temple." *Earthquake Spectra*, *33*(1_suppl), 377-384.

Yu, H., Mohammed, M. A., Mohammadi, M. E., Moaveni, B., Barbosa, A. R., Stavridis, A., and Wood, R. L. (2017). "Structural identification of an 18-story RC building in Nepal using post-earthquake ambient vibration and lidar data." *Frontiers in Built Environment*, *3*, p.11.

Zhang, W., Lin, P., Wang, N., Nicholson, C., and Xue, X. (2018). "Probabilistic Prediction of Postdisaster Functionality Loss of Community Building Portfolios Considering Utility Disruptions." *Journal of Structural Engineering*, American Society of Civil Engineers, 144(4), p.04018015.

Zhou, Z., Gong, J., and Hu, X. (2019). "Community-scale multi-level post-hurricane damage assessment of residential buildings using multi-temporal airborne LiDAR data." *Automation in Construction*, Elsevier, 98, 30–45.

Table 1: Summary of the traditional instruments used in each building.

Instrument type	Number	Description
Building A		
Uniaxial accelerometer	16	Two transverse at the edges, one longitudinal and one vertical in the middle of each floor slab and the roof
Building B		
Uniaxial accelerometer	16	Two transverse at the edges, one longitudinal and one vertical in the middle of each floor slab and the roof
Triaxial accelerometer	2	One on the soil box surface and one on the piping inside the soil box
LVDT	4	One at each corner of the building in the vertical direction

Table 2: Buildings foundation condition and shaking intensities at each test day.

<table>
<tr><th rowspan="3">Building ID</th><th colspan="2">Test day 1</th><th colspan="2">Test day 2</th><th colspan="2">Test day 3</th><th colspan="2">Test day 4</th></tr>
<tr><th colspan="8">Testing Configuration Variables</th></tr>
<tr><th>Base condition</th><th>Shaking intensities</th><th>Base condition</th><th>Shaking intensities</th><th>Base condition</th><th>Shaking intensities</th><th>Base condition</th><th>Shaking intensities</th></tr>
<tr><td>Building A</td><td>Base-isolation</td><td rowspan="2">JMA 25%
JMA 50%
JR 25%
JR 50%</td><td>Base-isolation</td><td rowspan="2">JMA 100%
JR 100%</td><td>Fixed</td><td>JMA 25%
JMA 50%</td><td>Fixed</td><td rowspan="2">JMA 100%</td></tr>
<tr><td>Building B</td><td>Soil-box</td><td>Soil-box</td><td>Soil-box with cast iron plates</td><td>JMA 100%
JR 100%</td><td>Fixed</td></tr>
</table>

JMA=Kobe – Japan Meteorological Agency record
JR=Takatori – Japan Railway record

Table 3: Details of scanning operations conducted before, during, and after each test day.

Day of testing	**Shaking phase**	**Interior or Exterior**	**Number of scanning stations**
Before tests outside the laboratory	No shaking	Interior and exterior using close-range scanner	61
Before tests after buildings placed on the shake table	No shaking	Interior	40
		Exterior	22
Day 1	After JMA 50% (see Table 2)	Exterior	11
	After JR 50% (see Table 2)	Interior	39
		Exterior	19
Day 2	After JMA 100% (see Table 2)	Exterior	9
	After JR 100% (see Table 2)	Interior	45
		Exterior	19
Day 3	Pre-test (reference)	Exterior	9
	After JR 100% (see Table 2)	Interior	46
		Exterior	18
Day 4	After JMA 100% (see Table 2)	Interior	5
		Exterior	33

Table 4: The façade damage measurements detected using LiDAR scans on test day 3.

Building A				**Building B**	
Cracks		*Damaged areas*		*Cracks*	
Label	Length (m)	Label	Area (m^2)	Label	Length (m)
A-E-2	0.545	A-E-1	1.679	B-E-1	0.266
A-E-3	1.010			B-E-2	0.527
A-E-4	1.610			B-W-1	1.148
A-E-5	0.878			B-W-2	0.538
A-E-6	0.768				
A-W-1	0.550				
A-W-2	0.798				

Table 5: Façade damage measurements detected using LiDAR scans on test day 4.

Building A				**Building B**					
Cracks		*Damaged areas*		*Cracks*		*Damaged areas*		*Distorted column*	
Label	Length (m)	Label	Area (m^2)	Label	Length (m)	Label	Area (m^2)	Label	Angle (degree°)
A-E-1	1.611	A-E-2	3.125	B-E-1	0.840	B-W-3	0.659	B-W-6	9.880
A-E-4	1.019	A-E-3	2.500	B-E-2	0.914	B-W-7	1.278		
A-E-5	1.220	A-E-14	2.025	B-E-3	0.458				
A-E-6	1.924			B-E-4	0.608				
A-E-7	1.945			B-E-5	0.337				
A-E-8	1.684			B-E-6	1.485				
A-E-9	0.968			B-W-1	1.600				
A-E-10	1.539			B-W-2	0.561				
A-E-11	0.594			B-W-4	1.506				
A-E-12	1.394			B-W-5	0.997				
A-E-13	0.904								
A-W-1	1.443								
A-W-2	1.487								
A-W-3	0.500								

Figure 1: Photographs of the two wood residential buildings tested in this study from the four corners of the shake table: (a) Southeast, (b) Northeast, (c) Northwest, and (d) Southwest.

Figure 2: Building A elevation view: (a) north side, (b) west side, (c) south side, and (d) east side.

Figure 3: Building A architectural layout floor plans for: (a) story 1, (b) story 2, and (c) story 3.

Figure 4: Wood bracing details of Building A at each cross section.

Figure 5: LiDAR scanners used: (a) close-range scanner to scan building interiors, (b) long-range scanner to scan building exteriors (view from the south-side observation deck level 2).

Figure 6: Accelerometer locations on each floor of Buildings A and B.

Figure 7: (a) and (b) JMA 100% record in x and y directions, and (c) and (d) their calculated acceleration response spectra.

Figure 8: (a) and (b) JR 100% record in x and y directions, and (c) and (d) their calculated acceleration response spectra.

Figure 9: Overview of LiDAR scanning procedure for full-scale shake table tests.

Figure 10: Relative location of the interior scanning setups and target locations after test day 3.

Figure 11: A screenshot of the 3D point cloud of the two buildings using collected LiDAR scans.

Figure 12: Distorted column in Building B after test day 4: (a) a photograph taken by a camera and (b) a screenshot of the column from LiDAR point clouds.

Figure 13: Damage to two wood bracing elements on (a), (b) the east side, and (c), (d) the west side; (a) and (c) are camera photographs, and (b) and (d) are screenshots of the collected LiDAR point clouds.

Figure 14: Façade damage detected using LiDAR scans after test day 3 on: (a) Building A east side, (b) Building A west side, (c) Building B east side, and (d) Building B west side.

Figure 15: Façade damage detected using LiDAR scans after test day 4 on: (a) Building A east side, (b) Building A west side, (c) Building B east side, and (d) Building B west side.

Figure 16: East side interior walls of Building A after test day 3.

Figure 17: Close-up view of sections (a) A and (b) B from Figure 16 – Building A, test day 3.

Figure 18: Damage detected on the Building A – east side exterior façade using cloud to cloud comparison.

Figure 19: Time history of recorded motion on shake table and displacement measurements using traditional instruments at the corners of Building B: (a) southwest, (b) southeast, (c) northwest, and (d) northeast corners.

Figure 20: Screenshot of point clouds of Building B before (red point clouds) and after (white point clouds) JMA 100% shaking on test day 2 and measurements (in mm) using LiDAR scans (shown in green) and traditional instruments (shown in yellow).

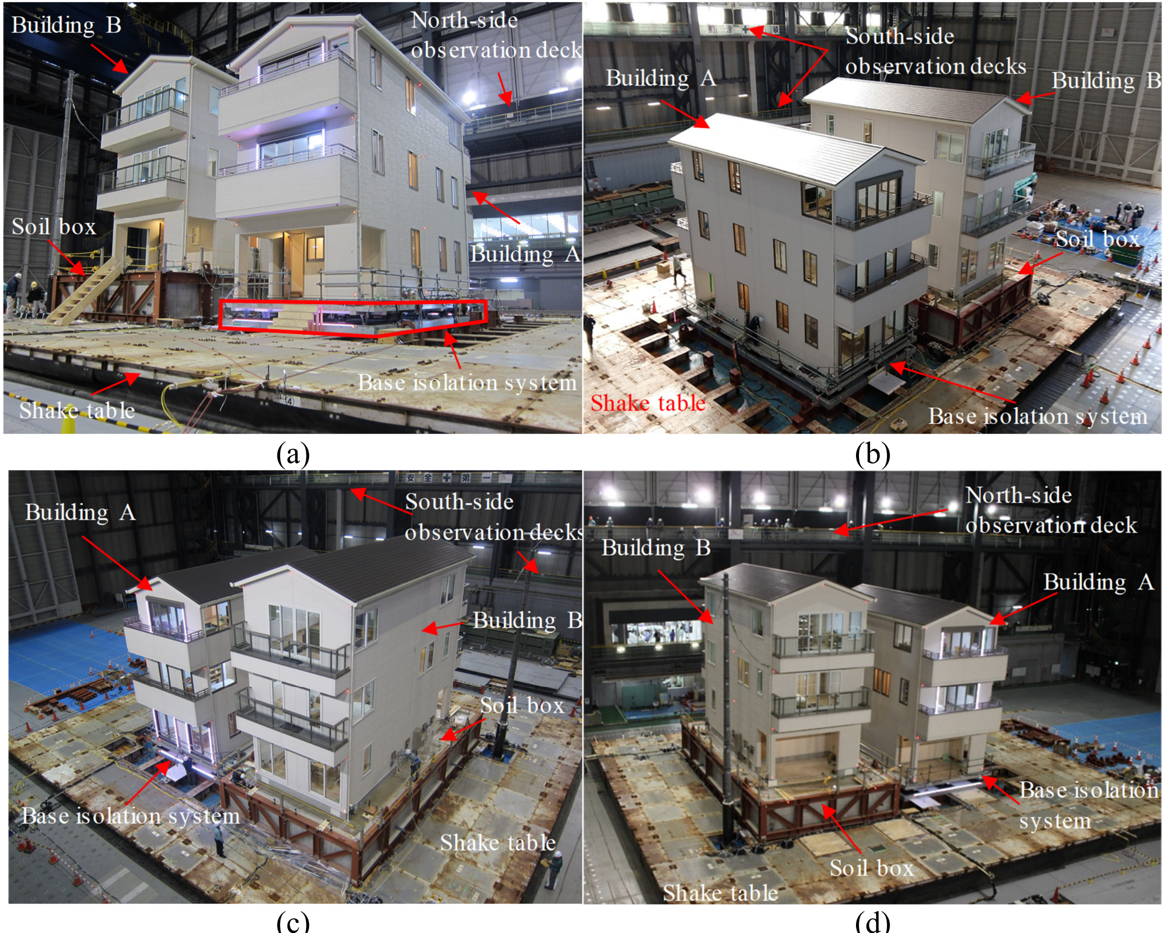

Building B
North-side observation deck
Soil box
Building A
Base isolation system
Shake table
(a)
South-side observation decks
Building A
Building B
Soil box
Shake table
Base isolation system
(b)
Building A
South-side observation decks
Building B
Soil box
Base isolation system
Shake table
(c)
North-side observation deck
Building B
Building A
Base isolation system
Soil box
Shake table
(d)

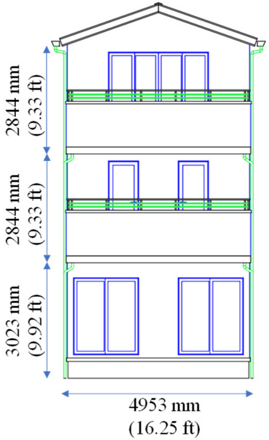
2844 mm
(9.33 ft)
2844 mm
(9.33 ft)
3023 mm
(9.92 ft)
4953 mm
(16.25 ft)

(a)

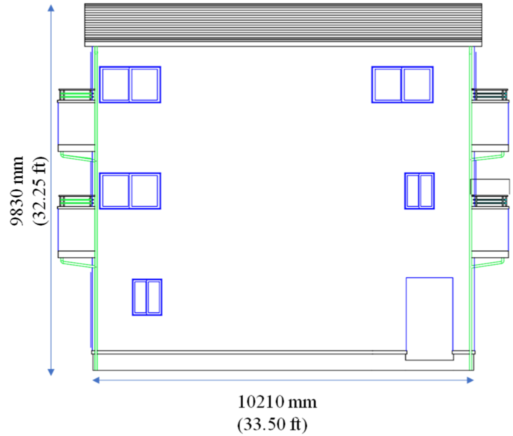
9830 mm
(32.25 ft)
10210 mm
(33.50 ft)

(b)

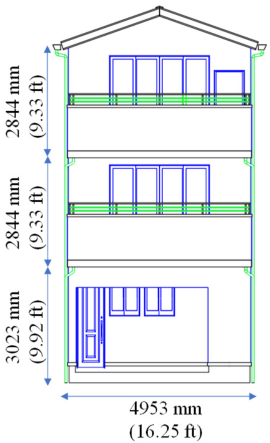
2844 mm
(9.33 ft)
2844 mm
(9.33 ft)
3023 mm
(9.92 ft)
4953 mm
(16.25 ft)

(c)

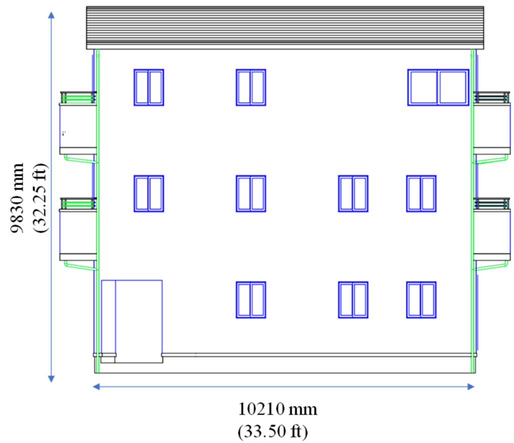
9830 mm
(32.25 ft)
10210 mm
(33.50 ft)

(d)

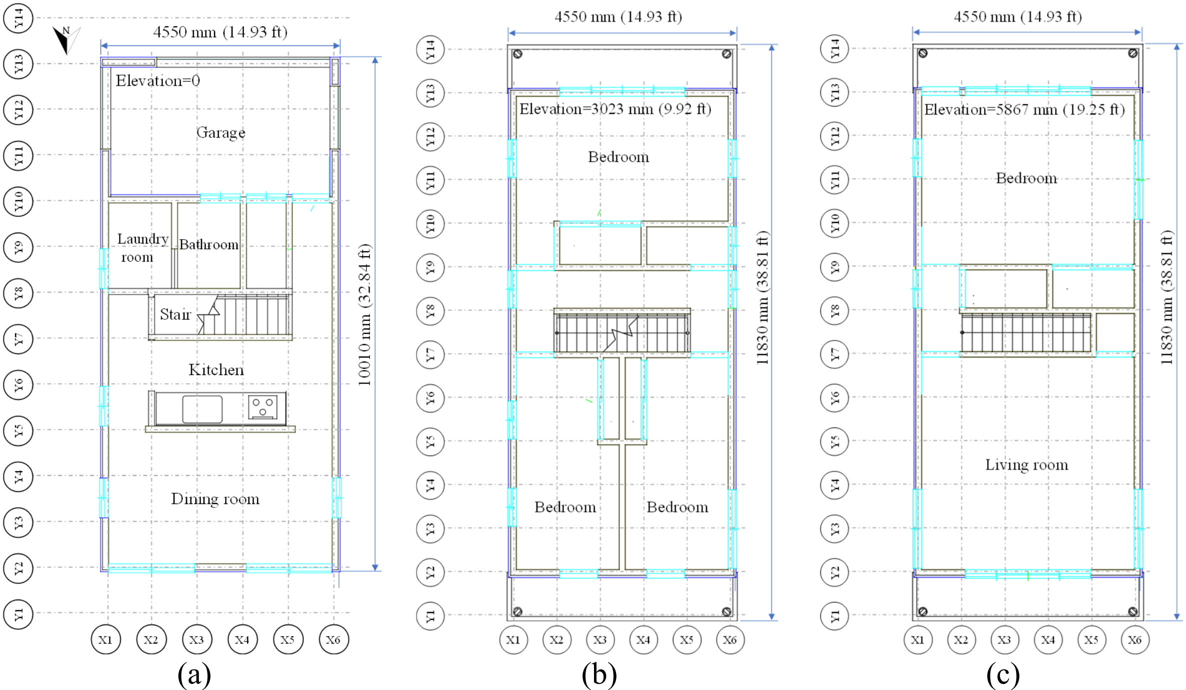
4550 mm (14.93 ft)
Elevation=0
Garage
Laundry room
Bathroom
Stair
Kitchen
Dining room
10010 mm (32.84 ft)
N
Y1
Y2
Y3
Y4
Y5
Y6
Y7
Y8
Y9
Y10
Y11
Y12
Y13
Y14
X1
X2
X3
X4
X5
X6
(a)
4550 mm (14.93 ft)
Elevation=3023 mm (9.92 ft)
Bedroom
Bedroom
Bedroom
11830 mm (38.81 ft)
(b)
4550 mm (14.93 ft)
Elevation=5867 mm (19.25 ft)
Bedroom
Living room
11830 mm (38.81 ft)
(c)

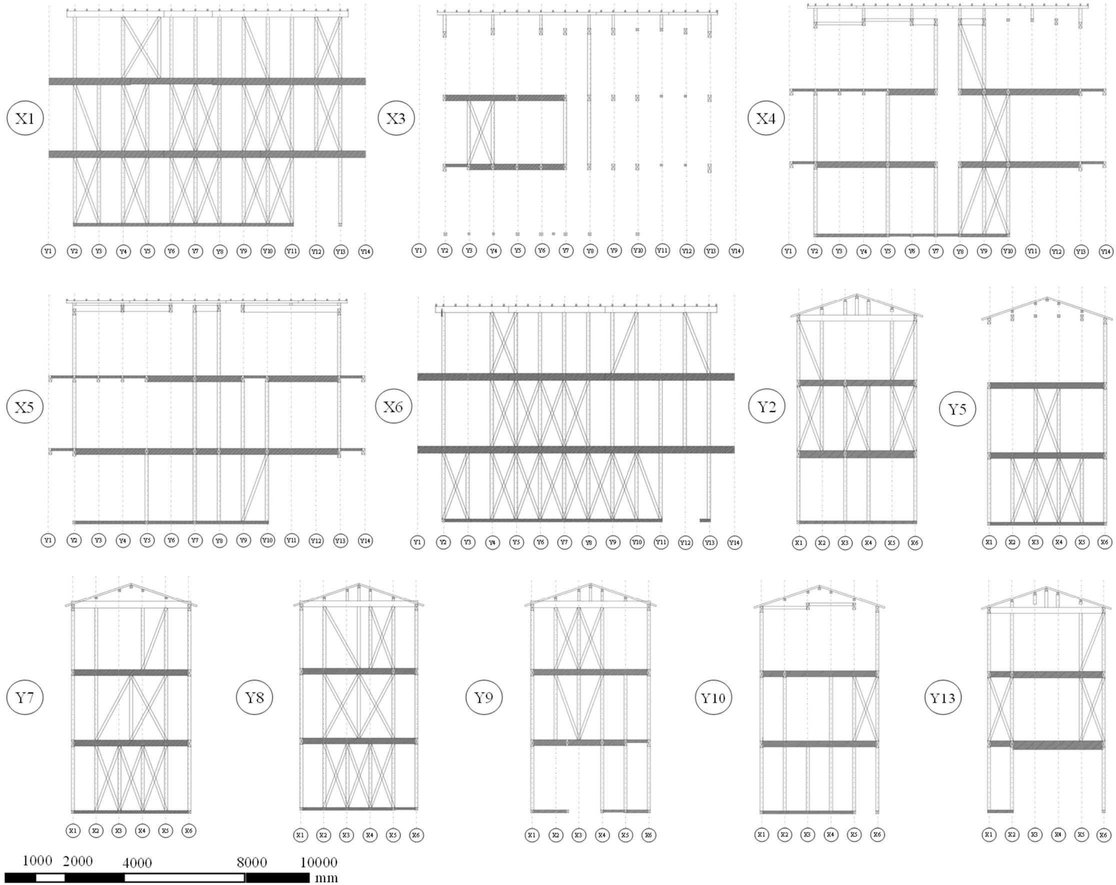
X1
X3
X4
X5
X6
Y2
Y5
Y7
Y8
Y9
Y10
Y13
1000
2000
4000
8000
10000
mm

(a) (b)

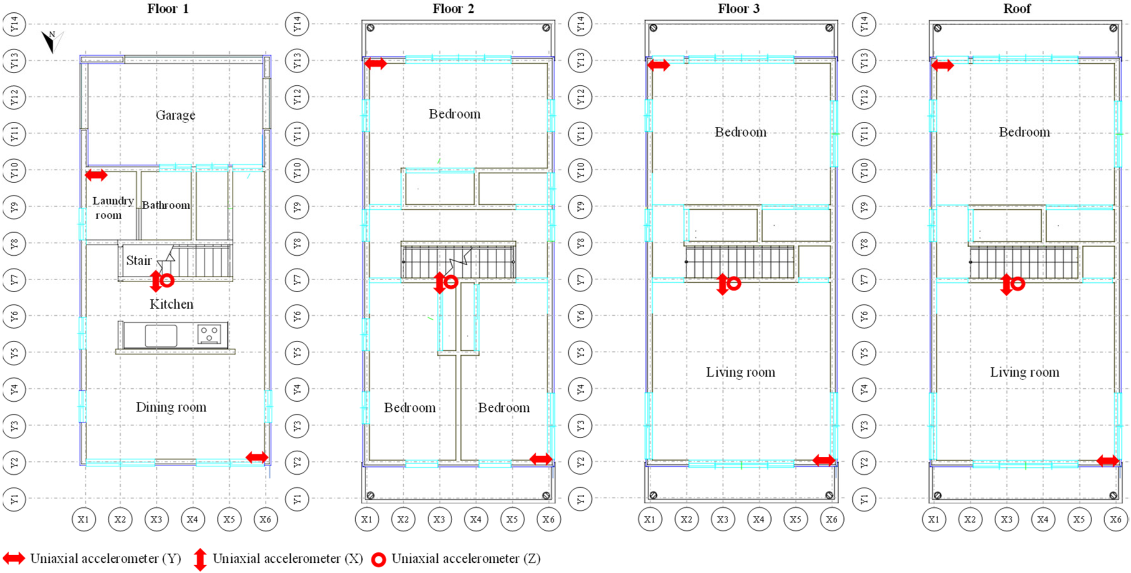
Floor 1
Floor 2
Floor 3
Roof
N
Garage
Laundry room
Bathroom
Stair
Kitchen
Dining room
Bedroom
Bedroom
Bedroom
Bedroom
Living room
Bedroom
Living room
Y1 Y2 Y3 Y4 Y5 Y6 Y7 Y8 Y9 Y10 Y11 Y12 Y13 Y14
X1 X2 X3 X4 X5 X6
Uniaxial accelerometer (Y)
Uniaxial accelerometer (X)
Uniaxial accelerometer (Z)

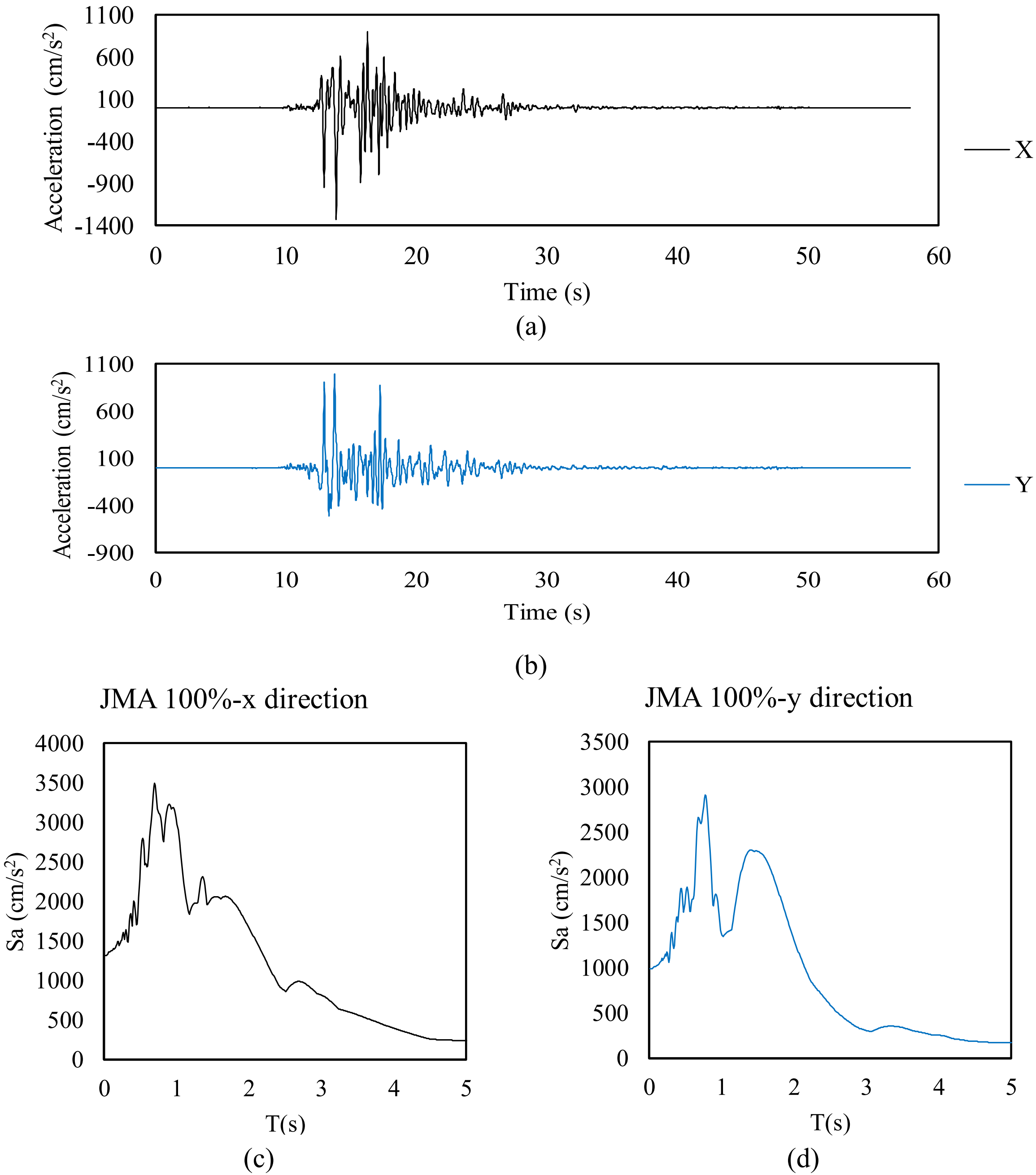

Acceleration (cm/s²)
1100
600
100
-400
-900
-1400
0
10
20
30
40
50
60
Time (s)
X
(a)
Acceleration (cm/s²)
1100
600
100
-400
-900
0
10
20
30
40
50
60
Time (s)
Y
(b)
JMA 100%-x direction
Sa (cm/s²)
4000
3500
3000
2500
2000
1500
1000
500
0
0
1
2
3
4
5
T(s)
(c)
JMA 100%-y direction
Sa (cm/s²)
3500
3000
2500
2000
1500
1000
500
0
0
1
2
3
4
5
T(s)
(d)

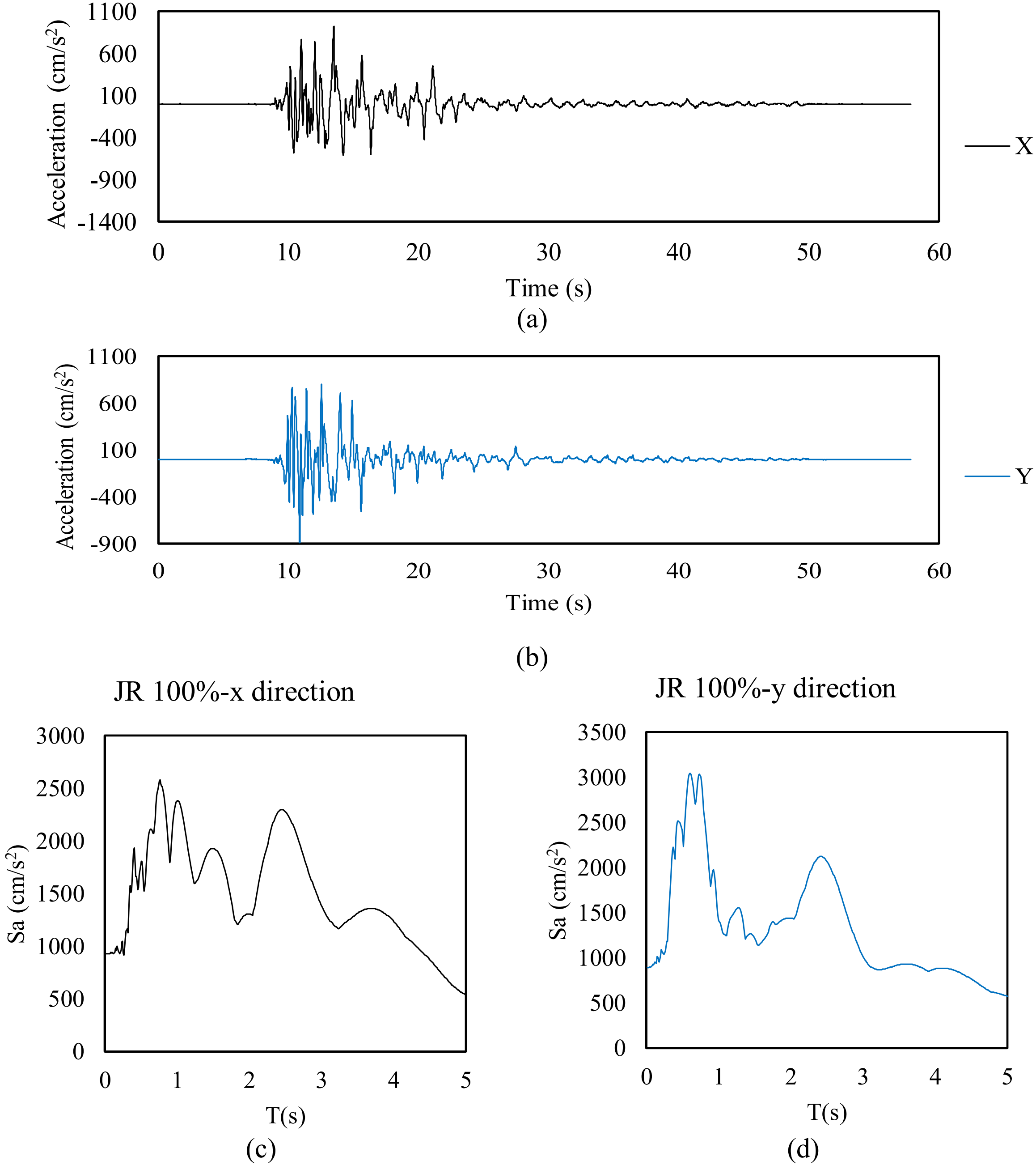
Acceleration (cm/s^2)
1100
600
100
-400
-900
-1400
0
10
20
30
40
50
60
Time (s)
X
(a)
Acceleration (cm/s^2)
1100
600
100
-400
-900
0
10
20
30
40
50
60
Time (s)
Y
(b)
JR 100%-x direction
Sa (cm/s^2)
3000
2500
2000
1500
1000
500
0
0
1
2
3
4
5
T(s)
(c)
JR 100%-y direction
Sa (cm/s^2)
3500
3000
2500
2000
1500
1000
500
0
0
1
2
3
4
5
T(s)
(d)

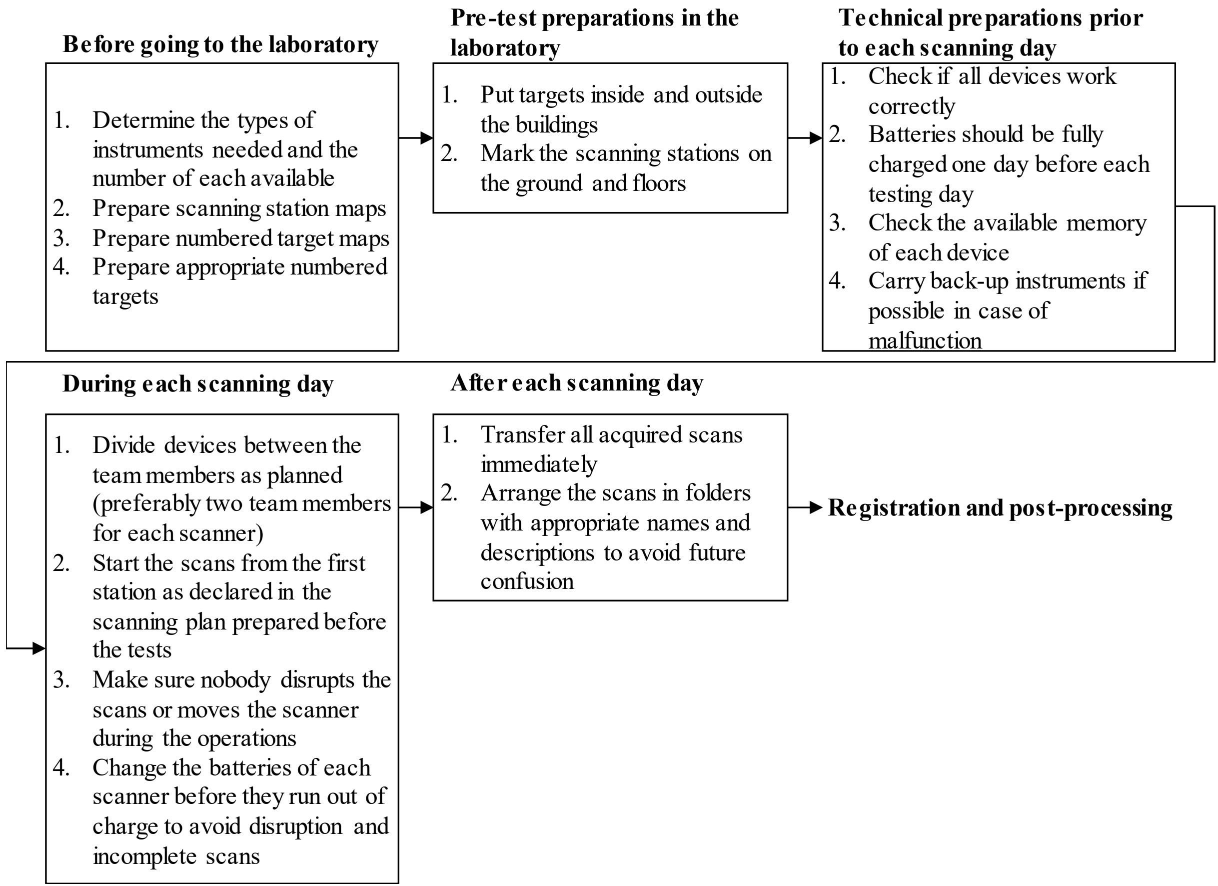
Before going to the laboratory
1. Determine the types of instruments needed and the number of each available
2. Prepare scanning station maps
3. Prepare numbered target maps
4. Prepare appropriate numbered targets
Pre-test preparations in the laboratory
1. Put targets inside and outside the buildings
2. Mark the scanning stations on the ground and floors
Technical preparations prior to each scanning day
1. Check if all devices work correctly
2. Batteries should be fully charged one day before each testing day
3. Check the available memory of each device
4. Carry back-up instruments if possible in case of malfunction
During each scanning day
1. Divide devices between the team members as planned (preferably two team members for each scanner)
2. Start the scans from the first station as declared in the scanning plan prepared before the tests
3. Make sure nobody disrupts the scans or moves the scanner during the operations
4. Change the batteries of each scanner before they run out of charge to avoid disruption and incomplete scans
After each scanning day
1. Transfer all acquired scans immediately
2. Arrange the scans in folders with appropriate names and descriptions to avoid future confusion
Registration and post-processing

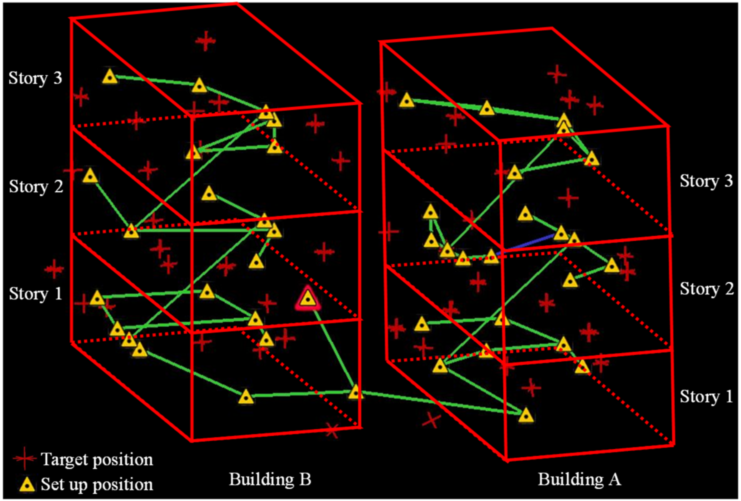

Story 3
Story 2
Story 1
Story 3
Story 2
Story 1
Target position
Set up position
Building B
Building A

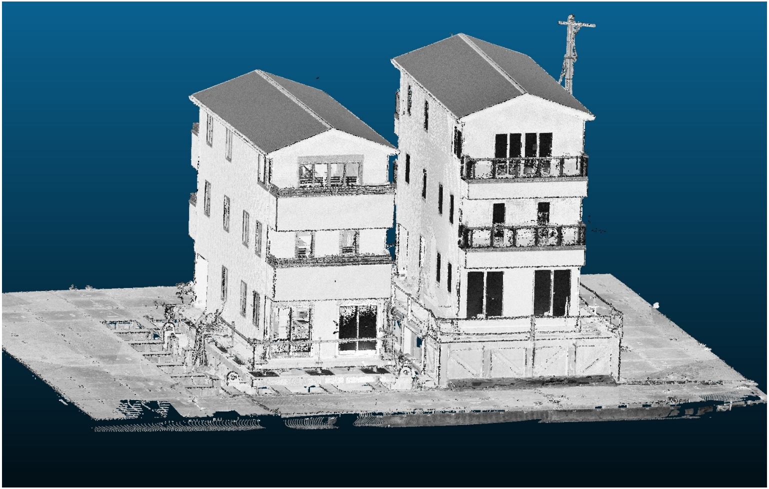

(a) (b)

(a)

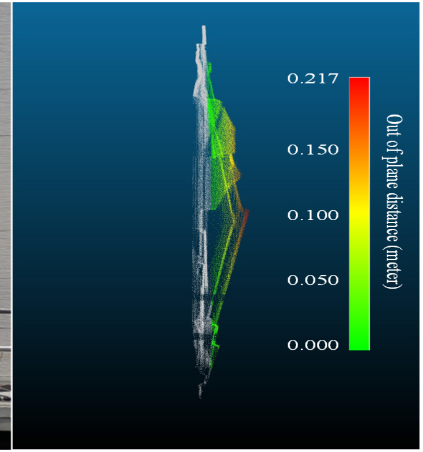
0.217
0.150
0.100
0.050
0.000
Out of plane distance (meter)

(b)

(c)


1.372 m
0.164 m
0.513 m
0.129 m

(d)

(a)

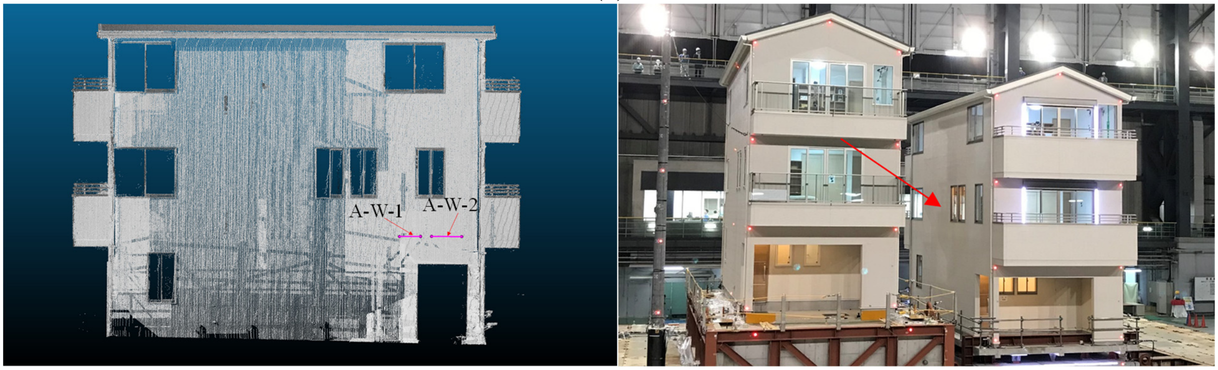

(b)

(c)

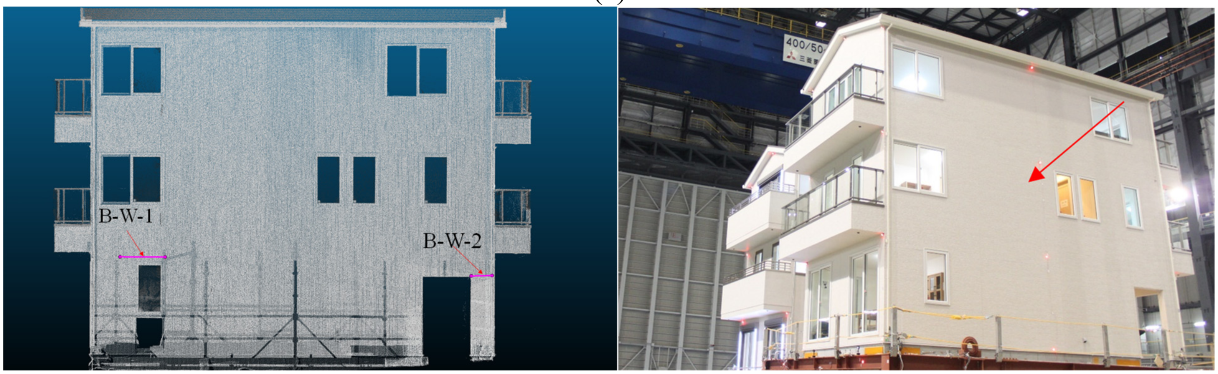

(d)

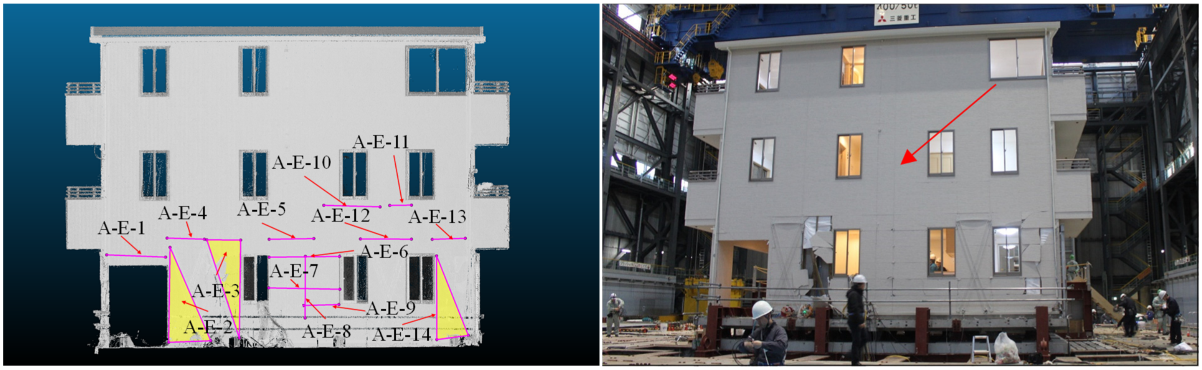
A-E-1
A-E-2
A-E-3
A-E-4
A-E-5
A-E-6
A-E-7
A-E-8
A-E-9
A-E-10
A-E-11
A-E-12
A-E-13
A-E-14

(a)

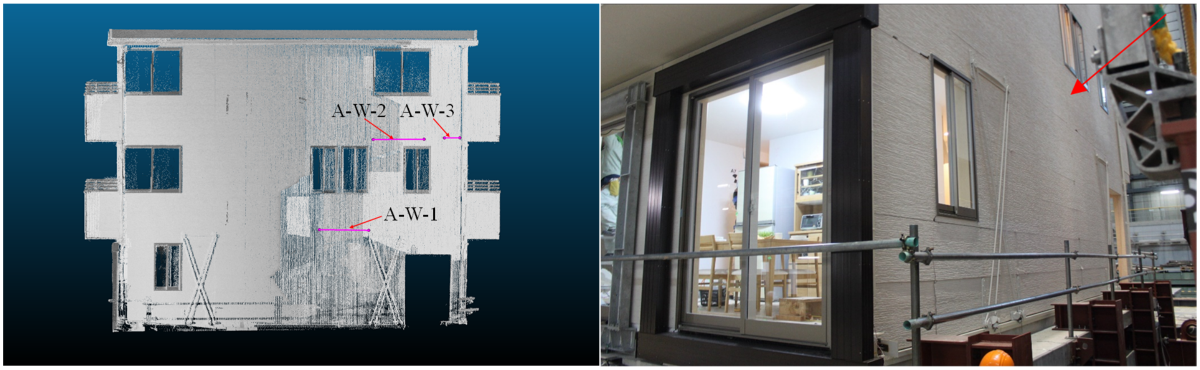
A-W-1
A-W-2
A-W-3

(b)

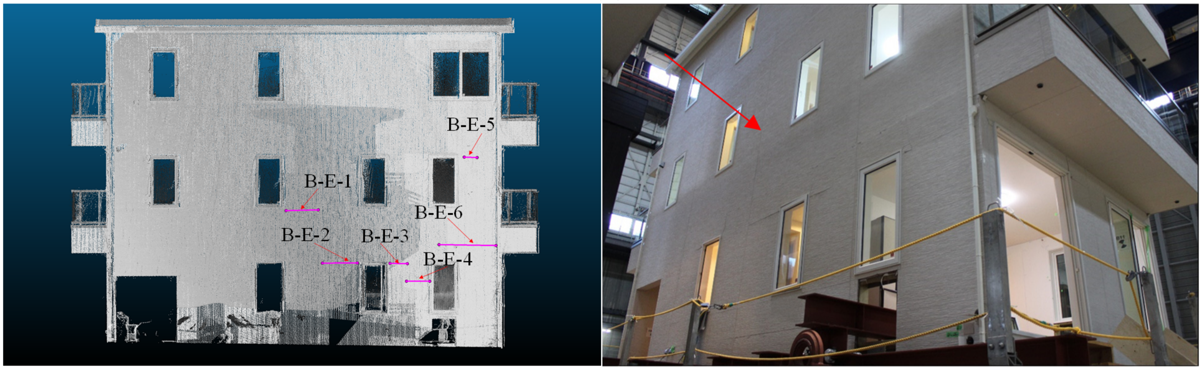
B-E-1
B-E-2
B-E-3
B-E-4
B-E-5
B-E-6

(c)


B-W-1
B-W-2
B-W-3
B-W-4
B-W-5
B-W-6
B-W-7

(d)


A24
B3
A13
A12
A16
Section B
A6
A4
Section A

(a)


A6
A7
A8
Crack (1.32m)
Spalling
Spalling
Crack (2.32m)

(b)

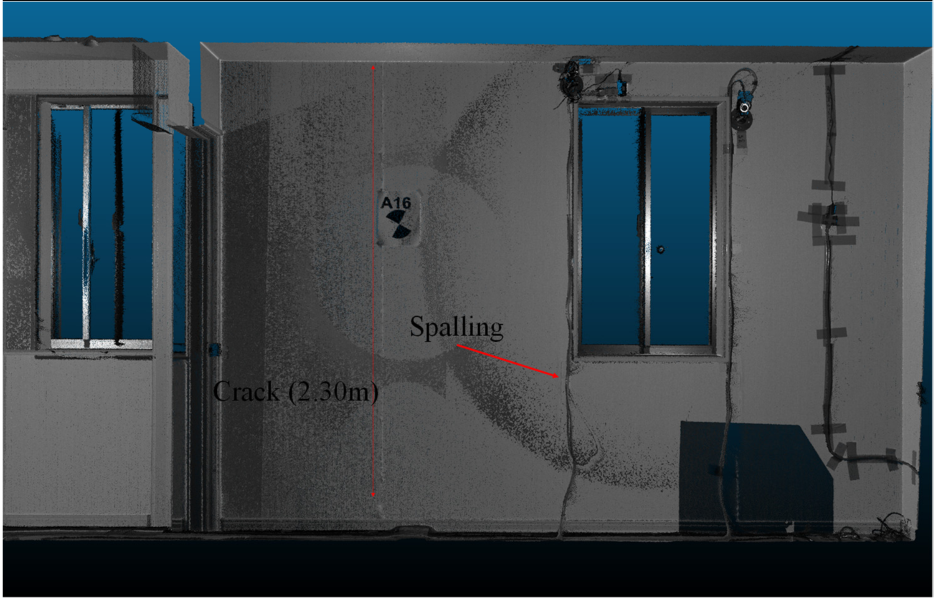
A16
Spalling
Crack (2.30m)

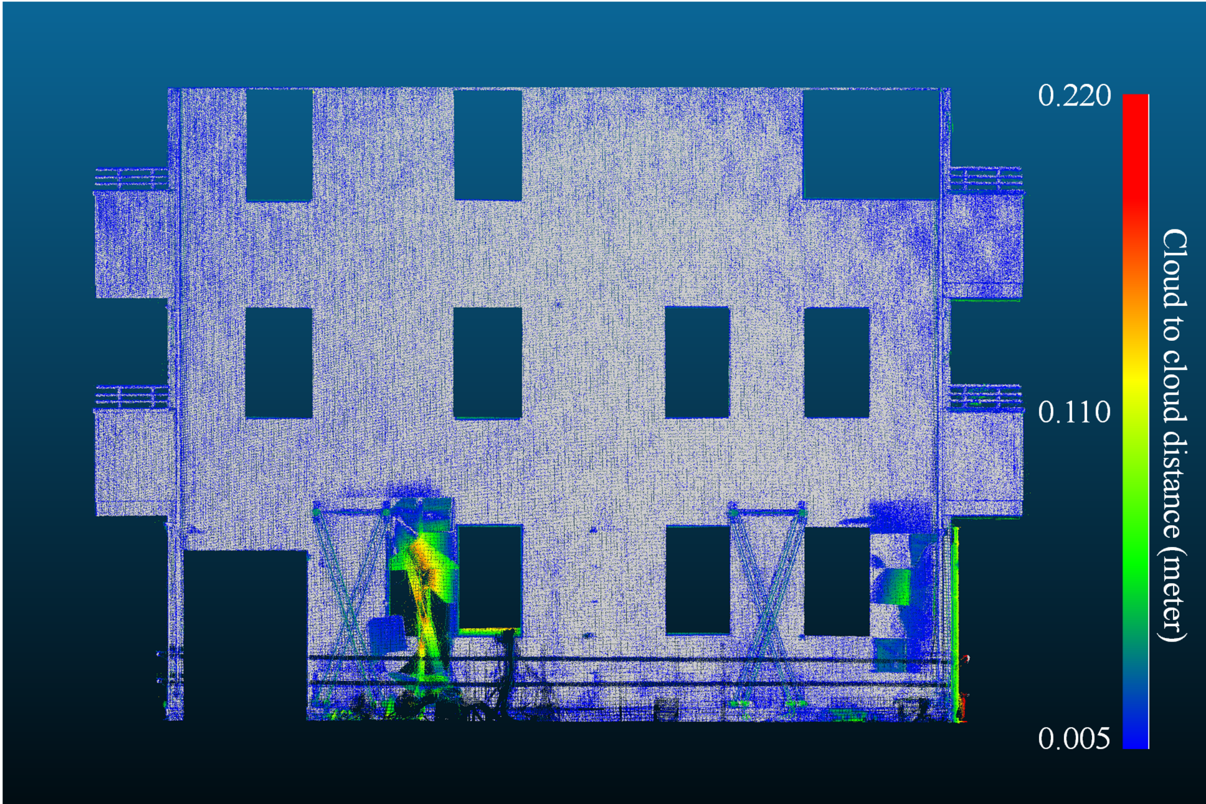

0.220
0.110
0.005
Cloud to cloud distance (meter)

Figure 19 Click here to access/download;Figure;Figure 19.pdf

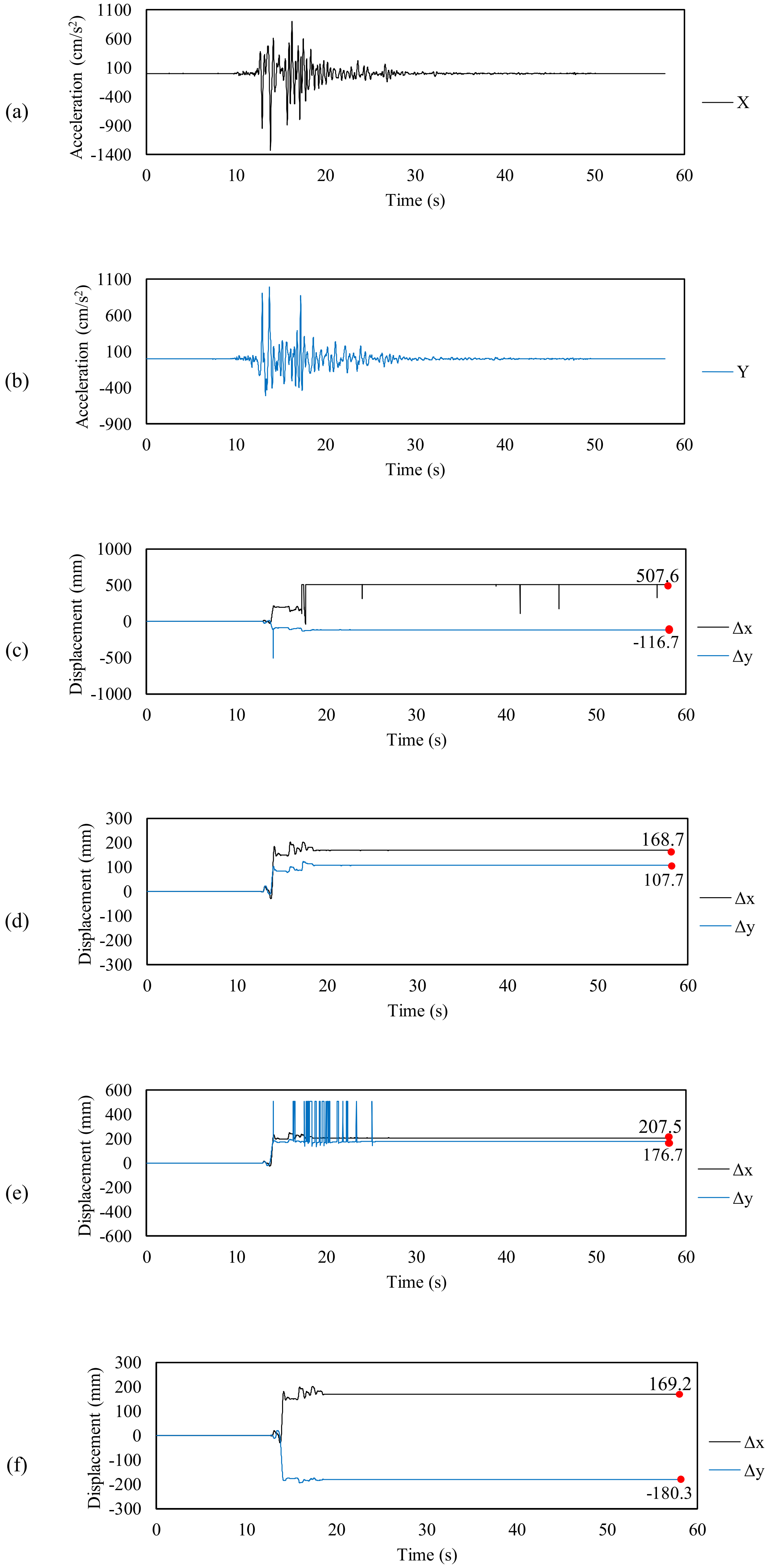

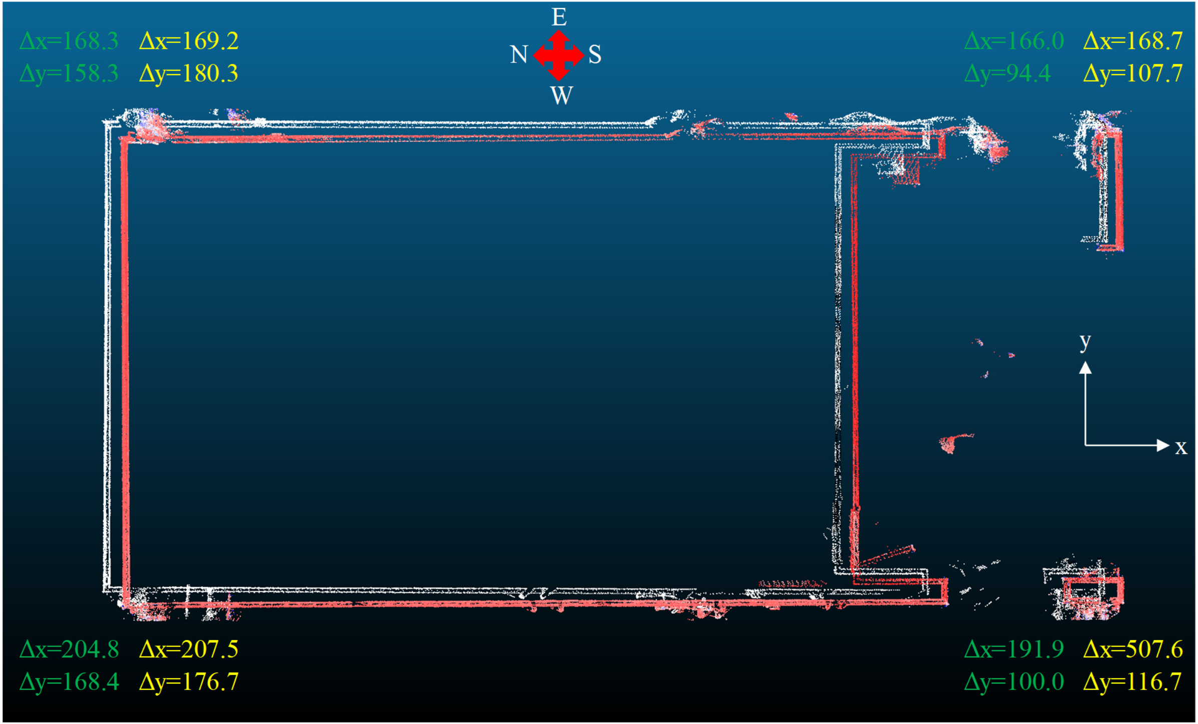

Δx=168.3 Δx=169.2
Δy=158.3 Δy=180.3
E
N
S
W
Δx=166.0 Δx=168.7
Δy=94.4 Δy=107.7
y
x
Δx=204.8 Δx=207.5
Δy=168.4 Δy=176.7
Δx=191.9 Δx=507.6
Δy=100.0 Δy=116.7

Figure 1: Photographs of the two wood residential buildings tested in this study from the four corners of the shake table: (a) Southeast, (b) Northeast, (c) Northwest, and (d) Southwest.

Figure 2: Building A elevation view: (a) north side, (b) west side, (c) south side, and (d) east side.

Figure 3: Building A architectural layout floor plans for: (a) story 1, (b) story 2, and (c) story 3.

Figure 4: Wood bracing details of Building A at each cross section.

Figure 5: LiDAR scanners used: (a) close-range scanner to scan building interiors, (b) long-range scanner to scan building exteriors (view from the south-side observation deck level 2).

Figure 6: Accelerometer locations on each floor of Buildings A and B.

Figure 7: (a) and (b) JMA 100% record in x and y directions, and (c) and (d) their calculated acceleration response spectra.

Figure 8: (a) and (b) JR 100% record in x and y directions, and (c) and (d) their calculated acceleration response spectra.

Figure 9: Overview of LiDAR scanning procedure for full-scale shake table tests.

Figure 10: Relative location of the interior scanning setups and target locations after test day 3.

Figure 11: A screenshot of the 3D point cloud of the two buildings using collected LiDAR scans.

Figure 12: Distorted column in Building B after test day 4: (a) a photograph taken by a camera and (b) a screenshot of the column from LiDAR point clouds.

Figure 13: Damage to two wood bracing elements on (a), (b) the east side, and (c), (d) the west side; (a) and (c) are camera photographs, and (b) and (d) are screenshots of the collected LiDAR point clouds.

Figure 14: Façade damage detected using LiDAR scans after test day 3 on: (a) Building A east side, (b) Building A west side, (c) Building B east side, and (d) Building B west side.

Figure 15: Façade damage detected using LiDAR scans after test day 4 on: (a) Building A east side, (b) Building A west side, (c) Building B east side, and (d) Building B west side.

Figure 16: East side interior walls of Building A after test day 3.

Figure 17: Close-up view of sections (a) A and (b) B from Figure 16 – Building A, test day 3.

Figure 18: Damage detected on the Building A – east side exterior façade using cloud to cloud comparison.

Figure 19: Time history of recorded motion on shake table and displacement measurements using traditional instruments at the corners of Building B: (a) southwest, (b) southeast, (c) northwest, and (d) northeast corners.

Figure 20: Screenshot of point clouds of Building B before (red point clouds) and after (white point clouds) JMA 100% shaking on test day 2 and measurements (in mm) using LiDAR scans (shown in green) and traditional instruments (shown in yellow).